Investigation on thermal management performance of PCM-fin structure for Li-ion battery module in high-temperature environment

Ping Ping[a,c], Rongqi Peng[b], Depeng Kong[b,1*], Guoming Chen[b], Jennifer Wen[c,*]

[a] *College of Chemical Engineering, China University of Petroleum (East China), Qingdao 266580, P R China*

[b] *College of Mechanical and Electronic Engineering, University of Petroleum of China, Qingdao 266580, PR China*

c Warwick FIRE, School of Engineering, University of Warwick, Library Road, Coventry CV4 7AL, UK

Abstract

The safety, performance and durability of the Li-ion battery module are limited by the operating temperature especially in the hot temperature regions, hence the thermal management system is essential for battery module. In this paper a novel phase change material (PCM) and fin structure was proposed for the thermal management system of $LiFePO_4$ battery module to reduce the maximum temperature and improve the temperature uniformity in high-temperature environment (40℃). Carefully designed experiments were performed for model validation. The effects of PCM species, fin thickness, fin spacing and PCM thickness on the cooling performance of battery module were investigated numerically. The results showed that PCM-fin structure thermal management system with optimized design exhibited good thermal performance, keeping the maximum temperature of the battery surface under 51℃ at relatively high discharge rate of 3C. Moreover, by investigating the thermal behavior of PCM during discharge process and cycle test, it has been found that PCM-fin structure has the advantage of improving natural convection and heat conduction within the PCM structure, and as a result enhance heat dissipation efficiency and reduce failure risk in passive thermal management systems using PCMs.

Keywords:

PCM; Fin; PCM-fin structure; Li-ion battery; thermal management; high temperature

[1] * Corresponding author, E-mail address: Jennifer.wen@warwick.ac.uk(J. Wen), kongdepeng@upc.edu.cn (D. Kong)

Nomenclature

		Greek symbols	
A	area, m^2		
a	charge transfer coefficients	κ	electric conductivity, S m^{-1}
a_s	specific interfacial area of the electrode, m^{-1}	ϕ	potential, V
		ε	volume fraction of a phase
c	lithium ion concentration, mol m^{-3}	Λ	molecular mean free path, m
C_p	heat capacity, J kg^{-1} K^{-1}	η	activation over-potentials of an electrode reaction, V
D	diffusion coefficient of lithium ion, m^2 s^{-1}	ρ	effective density of the active battery material, kg m^{-3}
E	cell potential, V		
E_{oc}	equilibrium potential, V	*Subscripts*	
f	mean molar activity coefficient of the electrolyte	0	reference quantity
F	Faraday's constant, 96.485 C mol^{-1}	1,2	surface 1, 2 quantity
H_{mic}	micro-hardness, Pa	*a*	apparent quantity
i_0	exchange current density of an electrode reaction, A m^{-2}	*b*	battery
		e	the electrolyte phase
J	transfer current resulted from the intercalation or deintercalation of lithium, A m^{-3}	*g*	gas, air
		neg	negative electrode
		pos	positive electrode
k	thermal conductivity, W m^{-1} K^{-1}	*sep*	electrolyte
K	electrochemical reaction rate constant, m s^{-1}	*neg_cc*	negative current collector
		pos_cc	positive current collector
M	gas parameter, m	*s*	the solid phase
L	thickness of the different layers of the cell, m	*l*	the liquid phase
		oc	open circuit
n_s	number of micro contacts	*rev*	reversible
R	thermal resistance, K W^{-1}	*rxn*	irreversible
R_c	the gas constant, 8.3143 J mol^{-1} K^{-1}	*j*	X, Y, Z-direction
r_s	radius of the spherical particle, m		
T	temperature, K	*Superscripts*	
t_+^0	transport number		
Y	mean surface plane separation, m	*eff*	effective

1. Introduction

Under the pressure of green-house gas and energy shortage, the electrification of transport plays an important role to meet the objective of the Paris Agreement enforced in November 2016. With high specific energy, long cycle-life and low self-discharge rate, Li-ion batteries (LIBs) are normally used as the energy supporting device integrated within electric vehicles (EVs) and hybrid electric vehicles (HEVs). Thanks to improvement in battery technologies and vigorous support by the governments, EVs employing LIBs are cannibalizing the market share of conventional fuel powered vehicles. A recent 2018 report by Frost & Sullivan highlighted that the market has reached the 1.2 million sales mark for the first time [1]. In China, there is a goal for EVs to account for 20% of vehicle sales by 2025 according to a car development guideline released from government [2]. The International Energy Agency (IEA) also forecasts that the EV stock is projected to reach 4 million units by 2030 based on the current market development in *Nordic EV outlook 2018* [3].

Although EVs continue to surge ahead in top gear, there are some challenges including the life as well as the dynamic performance of the vehicle, which leads to EVs have not been widely adopted by consumers. In view of the battery has a high energy density but a low power density, the use of other energy storage elements with high power density could complement the battery to sustain the high power needed for relatively short durations [4]. The energy storage element could be a flywheel or a super capacitor, they are also used in many fields including Solar photovoltaic (PV) [5] and wind energy systems [6,7]. To manage the intermittency produced by the wind turbine generator, super capacitor is used as energy storage or combined with the battery into the hybrid energy storage system (HESS) for a doubly fed induction generator (DFIG) [8, 9]. For example, Döşoğlu et al. [10] proposed the combination of the super capacitor and static synchronous compensator could maintain the wind farm bus voltage within desired limits during a fault of the power system.

For the Li-ion battery itself, one of the most significant factors affecting the safety, immediate performance and lifespan is the operating temperature. In general, high temperature caused by the continuous heat accumulation in cells during cycling accelerates the depletion of running battery materials and increases the risk of thermal runaway [11-13]. Väyrynen and Salminen et al. [14] suggested that the acceptable operating temperature for LIB is -20℃ to 60℃. In addition, the temperature gradient among cells in module is also of great concern. Yang et al. [15] investigated the

effect of temperature non-uniformity between cells and demonstrated that the unbalanced discharging and the ageing rate in battery is appreciably increasing as the temperature difference among cells increases. In order to avoid severe temperature gradient, the maximum temperature difference in a module should not exceed 5℃ [16]. As such, to relieve the rapid temperature rises whilst limiting the temperature distribution, a qualified and feasible battery thermal management (BTM) is essential for the battery module to ensure the safety, performance and durability of the battery.

In consideration of these requirements, numerous efforts have been devoted to design more efficient and advanced BTM systems which can be classified into several types based on the terms of cooling medium such as air cooling [17-19], liquid cooling [20-22], phase change material (PCM) cooling and the combination of them. With its simple structure, light weight and low cost, air cooling can provide an effective cooling performance in most cases, but the poor thermal conductivity of air constrains the applications in extreme environment or abuse conditions [23]. Comparing to air cooling, liquid cooling which has a higher thermal conductivity is a more attractive option for BTM. But its need for the circulation of coolants would increase structure complexity and the parasitic power costs for battery module need to be addressed to facilitate wide practical application. As an innovative solution for BTM system, PCM cooling utilizing latent heat during the phase change process can be traced back to Selman's work [24] which revealed that the paraffin PCM showed a much better thermal performance than conventional BTM systems. Therefore, PCM thermal management systems receive extensive attention and exploration in recent years due to the characteristics such as simplicity, low cost and stable chemical property.

Although considered as the most promising potential alternative of the traditional BTMs [25, 26], PCM such as the paraffin is significantly constrained because of its low thermal conductivity (normally less than 0.4 W m^{-1} K^{-1}) which determines the thermal efficiency. Therefore considerable research efforts have been invested to improve the effective thermal conductivity of PCM. One method is suspending thermally conductive fillers into PCMs. Carbon fiber, discussed by Samimi et al. [27], was added into paraffin which enhances the thermal conductivity (105% average enhancement); and the thermal performance of mixtures was beyond the air and pure PCM cooling. In addition to adding fillers, saturating PCMs into porous media is also a potential method, such as aluminum foam and expanded graphite (EG) matrix, which can create the thermal conductive networks [28]. Al-Hallaj et

al. [29] designed the combination of aluminum foam and PCM and applied it into LIB module. Results indicated the enhancement of PCM on the thermal performance by adding aluminum foam led a significant temperature drop of about 50% compared to natural convection cooling. It is worthy to note that utilizing EG matrix not only can enhance the thermal conductivity, but also reduces the leaking after the paraffin melts due to its capillary forces. Jiang et al. [30] embedded the paraffin into the EG and reported that an EG loading fraction of 30 wt% raise the PCM thermal conductivity to 13.85 W m^{-1} K^{-1}, while the leakage ratio was significantly decreased to 0.38 wt%. Therefore, the enhanced thermal conductivity and ability to prevent leakage after PCM melts render the porous matrix a promising alternative for BTMs application with increasing demands for the utilization of Li-ion batteries in abuse condition. However, a potential problem that should be taken into accounts is that the repeated melting/solidifying process might induce inhomogeneity or even module crack of the composite PCMs [31, 32].

In addition to the aforementioned techniques, finned structure as a highly efficient heat transfer device with excellent characteristics such as enhancement of the heat exchange area, simplicity of framework and ease of fabrication, has been widely used to enhance PCM heat storage for applications such as electronic equipment [33], space and solar thermal storage [34-36]. In the field of latent heat thermal energy storage (LHTES), many studies [36-40] verified that the presence of fins which increase the heat transfer area of PCM can improve the thermal performance of LHTES system. Further, Mahmoud et al. [41] investigated a single cavity and different fins array in a PCM-based heat sink units. The results showed that increasing the number of fins could improve the heat distribution into the PCM, which is more significant at higher heating power levels. When it comes to the application of fin structure into the thermal management of LIB, the related study is still rare. Wang et al. [42] investigated the thermal behavior of a mock-up cylindrical battery with paraffin and fin structure through experimental measurements and benchmarking with other thermal management techniques. It is found that the PCM-fin system had advantages of good thermal performance with prolonged work time. However, to the best of our knowledge, the performance of PCM inserted fin configurations has not been systematic studied for real batteries, especially for battery modules. In addition, detailed optimization study for the design of PCM-fin structure within the battery module can have significant effect and should be further investigated to facilitate practical application.

The present study numerically investigated the thermal performance of a passive thermal management system combining PCM and fins designed for prismatic LIB module under 40 ºC. For model validation, carefully designed experiments were performed. A single battery was tested with four cooling methods including PCM-fin structure. The good consistency between the simulation results and the experiments data illustrates high accuracy of the model. Analysis to compare the thermal characteristics of the PCM-fin against the pure PCM, subjected to same rapid discharging conditions, was then conducted through numerical simulation on a 5-cell battery module. This was followed by parametric study in which the affecting factors such as PCM species, fin thickness, fin spacing and PCM thickness were changed systematically to optimize the BTM system. Finally, the charging-discharging cycle test to rank the feasibility and effectiveness of the PCM-fin structure against pure PCM and PCM/EG cooling approaches, was conducted.

2. Experimental methodology

2.1. Geometric construction

The passive thermal management system was designed in this work to estimate the thermal response and the heat dissipation performance of PCM-fin structure for prismatic battery during discharge process. A commercial 10Ah $LiFePO_4$ (LFP) battery was selected as the unit cell. Figure 1 shows the schematic of passive cooling system for the battery module. Five prismatic cells and PCM-fin structure were closely placed in an aluminum battery box. PCM-fin structure consisted of two parts, a specialized aluminum heat sink and the PCM. For the specialized heat sink, a certain number of straight fins were uniformly spaced between two baseplates. Among them, PCM was filled, and *h* represented the PCM thickness as shown in Fig. 1(b).

As high heat transfer coefficient of the aluminum and straight fins increase the heat exchange area of PCM [42], heat generated in the cells can be quickly absorbed by the PCM. The basic parameters of LFP battery and aluminum materials can be seen in Table 1. Three different paraffin waxes, n-docosane (PCM44), n-tetracosane (PCM50) and n-pentacosane (PCM54) were selected as the phase change materials. These three PCMs have close physical properties except their melting temperature, as shown in Table 2. The Multiphysics code COMSOL was utilized to simulate the thermal performance of the system.

2.2. Battery modeling

For a prismatic battery, the 1D-electrochemical and 3D-thermal coupling models have been developed through the finite element method (FEM). In this model, Pseudo Two-dimensional (P2D) model was employed to form the 1D-electrochemical part, in which only 1D transport from one electrode through the separator to the counter electrode was considered and it was assumed that the active solid phase material consists of mono-sized spherical particles [46]. Meanwhile, the chemical and electrochemical reactions in the internal components of the battery generate heat which results in the temperature increase of battery during cycling. Based on the theories as mentioned above, Table 3 summarizes the electrochemical reactions, the heat equilibrium equation and corresponding boundary conditions. Table 4 shows the values of material parameters used in this simulation.

For accounting the non-uniformity of temperature distribution to represent the non-uniform heat source of real battery, additional heat sources of electrode tabs were added in this study, which were respectively made of aluminum and copper. During the cycling process, the heat generation rate of Joule heat generated by tabs can be determined as follows [49]:

$$q_{Al\&Cu} = \frac{Q_{Al}}{V_{Al}} + \frac{Q_{Cu}}{V_{Cu}} = \frac{I^2 R_{Al}}{V_{Al}} + \frac{I^2 R_{Cu}}{V_{Cu}} \tag{1}$$

where $Q_{Al/Cu}$ and $V_{Al/Cu}$ are the heat generation rate and volume of electrode tabs; $R_{Al/Cu}$ is the resistance of electrode tabs. Hence, the total heat generation rate can be determined as follows:

$$Q = Q_{cell} + Q_{Al} + Q_{Cu} \tag{2}$$

2.3. Thermal contact resistance

When different materials come into contact, real contacts occur only at the top of the interfacing asperities which are called the micro-contacts [51]. The micro-contacts are generally located far from each other making the real contact area (a summation of all micro-contact areas) only a small portion of the nominal contact area [52]. Besides, the gaps between the micro-contacts are filled with interstitial air. The heat transfer between different materials can generally cause a significant temperature drop, which is called as thermal contact resistance (R_c) [53]. In this study, after batteries generating heat, PCM as the main heat-dissipating material was used to absorb heat conducted by the specialized aluminum heat sink. In order to improve the accuracy of this model, the thermal contact resistance which exists in the contacting surface of different materials was considered.

R_c contains three parts, i.e., the micro-contact resistance, the micro-gap thermal resistance and

the radiation heat resistance. In general, the micro-contact resistance and the micro-gap thermal resistance are the main thermal resistance, which cannot be neglected. It is acknowledged that the radiation heat resistance is insignificant if the surface temperatures are under 700K. Table 5 shows the detailed equations for the thermal contact resistance. It can be seen that the thermal contact resistance is mainly governed by the effective roughness, the interstitial air and the contact pressures. In this study, it is assumed that a single variable is the equivalent root-mean-squared (RMS) roughness effecting the values of R_c, while other factors are constant. Table 6 lists the parameters used to calculate the values of R_c.

2.4. PCM model

For the phase change materials region, the thermo-physical properties of PCM are dependent on the state of PCM. Thereinto, the specific heat capacity (C_p) of PCM can be described as follows:

$$C_p = \begin{cases} C_{PCMS} & T_{PCM} \le T_s \,(solid\ phase) \\ (1-\theta)C_{PCMS} + \theta C_{PCML} + \dfrac{L_{PCM}}{T_l - T_s} & T_s < T_{PCM} < T_l \,(solid\,/\,liquid\ phase) \\ C_{PCML} & T_{PCM} \ge T_l \,(liquid\ phase) \end{cases} \tag{3}$$

where C_{PCMS}, C_{PCML} and L_{PCM} are heat capacity of solid PCM, heat capacity of liquid PCM and latent heat of PCM. T_{PCM}, T_s and T_l respectively stand for the temperature of PCM, the initial temperature of phase transition and the end temperature of phase transition. θ represents the volume fraction of liquid PCM, which is described as follows:

$$\theta = \frac{T_{PCM} - T_s}{T_l - T_s}, if\ T_s < T_{PCM} < T_l \tag{4}$$

2.5. Initial conditions and boundary conditions

During the process of simulation, the initial state was specified as follows:

$$t = 0; T(x, y, z) = T_{amb}; \tag{5}$$

where T_{amb} is the ambient temperature.

Boundary condition at the interface between battery and baseplate of specialized aluminum heat sink relies on the energy conservation:

$$-k_b \frac{\partial T}{\partial n} = -k_{c,B-A} \frac{\partial T}{\partial n} - k_{Al} \frac{\partial T}{\partial n} \tag{6}$$

where k_b and k_{Al} are the thermal conductivity of battery and heat sink, $k_{c,B\text{-}A}$ is the thermal contact

conductivity between the battery and the aluminum baseplate, and $\frac{\partial \mathrm{T}}{\partial \mathrm{n}}$ represents temperature gradient.

The contact surface between straight fin of specialized aluminum heat sink share similar boundary condition:

$$-k_{Al}\frac{\partial T}{\partial n} = -k_{c,A-P}\frac{\partial T}{\partial n} - k_{PCM}\frac{\partial T}{\partial n} \tag{7}$$

where k_{PCM} is the thermal conductivity of PCM, $k_{c,A\text{-}P}$ the thermal contact conductivity between aluminum heat sink and PCM.

The energy equation at the boundary between the battery box and the ambient was given by:

$$-k_{box}\frac{\partial T}{\partial n} = h(T_{box} - T_{amb}) \tag{8}$$

where k_{box} and T_{box} represent the thermal conductivity and temperature of battery box, h is the natural convection heat transfer coefficient, whose value is 10 W m^{-2} K^{-1} in this simulation.

Before the numerical simulation, the sensitivity analysis of grid number on the simulation results was conducted. Three grid number, i.e., 433358, 893151 and 3095108 were used. Figure 2 shows the simulated maximum temperature responses of the battery surface within the module with PCM-fin structure at different gird numbers. It can be seen that there is almost no discrepancy between the numerical temperatures of the battery at different grid numbers, so the grid number of 433358 was used in this study to balance the computational costs and simulation accuracy.

2.6 Experimental

In order to verify the accuracy of the model in simulating the temperature variation, a 10 Ah LFP battery with same size as simulated cell was selected for this work. The discharge rates were 1C, 1.5C, 2C and 3C under different thermal management modes. Figure 3 illustrates the schematic of the experimental system to measure the thermal performance of single battery with PCM-fin structure. The battery was vertically put in the center of an aluminum box with the size of 160×145×68mm.

A pair of heat sinks with fins were directly attached to the battery, and PCM enwrapped the battery and heat sinks to form thermal enhancement structure. The box was placed in the thermostat incubator, for which the ambient temperature fluctuation was controlled within ±1 ºC. Other thermal management modes were the natural convection without PCM and heat sink, pure PCM and heat sink without PCM, respectively. It is noted that the experimental paraffin (purchased from Daqing Refining

& Chemical Co., Ltd, Daqing, China) was n-pentacosane as shown in Table 2.

Before the experiments, the liquid PCM was filled in the box which had installed the battery mold (or/and the heat sinks). The preliminary battery tests under the continuous 0.5C cycling were conducted by the battery cycler. 0.5mm K-type thermocouples with 1s response time and ±1.0 ºC accuracy were arranged on five different locations of battery (the tabs of electrode, near the top of battery, on the middle, near the bottom of battery) to record the temperature, as shown in Figure 4. Then, the battery took the place of the mold in the box after the solidification of the PCM.

During the experiments, the thermostat incubator temperature was set to 40℃. The ambient temperature was measured by a thermocouple inserted into the thermostat incubator. As shown in Fig. 4, all thermocouples lead wires were connected to the outside temperature acquisition module whose data was stored in the PC, through the reserved hole on the top of thermostat incubator. The 5 continuous charge-discharge cycles by the battery cycler was set as follows. For each cycle, the battery was first charged from 2.5V to 3.6V at 0.5C, then a constant voltage charge process was conducted with cutoff current of 30 mA. After laying-aside time of 40 min, the battery was discharged to 2.5V at different current rates. After the same laying-aside time, the first step was executed again until 5 cycles end.

3. Results and discuss

3.1. Battery model validation

Experiments and simulations were carried out for single cell contained in the aluminum box under different thermal management modes, natural convection without PCM and heat sink, pure PCM, heat sink without PCM, and PCM-fin structure. In order to reduce experimental measurement errors, the average temperature evolutions in five locations of the single cell were calculated among the 5 discharge cycles.

Figure 5 shows the comparisons of the inhomogeneous temperature contours and evolution history obtained from prediction and measure during 3C discharge. A significant decrease of the battery surface temperature was observed from natural convection to using the heat dissipation materials. The temperature of T3 for natural convection was 66.4 ºC, as shown in Fig. 5(a). Comparatively, the temperature of T3 in the case of heat sink without PCM was 56.1 ºC due to the improvement of the surface heat transfer capability, as indicated in Fig. 5(b). Attributing to the

characteristics of heat absorption with high latent heat, pure PCM module restricted the temperature of T3 under 54.9 ºC depicted in Fig. 5(c). However, PCM-fin structure module got the temperature of 51.6 ºC observed in Fig. 5(d), which was the lowest in four cases, and the temperature uniformity was also better than other modules. The main reason is the heat generated from battery can more quickly conduct to interior PCM owing to aluminum fin structure increasing the heat exchange area of PCM, while the pure PCM can only slowly conduct heat due to its low thermal conductivity. It can be clearly seen from Fig.5 that the predictions agree well with the experimental results, indicating the rationality of battery heat generation, thermal contact resistance and thermal management model used in simulation.

To further demonstrate the ability of the proposed design in terms of efficiency, effectiveness and accuracy in controlling the temperature of the battery, a series of experiments and numerical simulations were conducted for different discharge conditions. Figure 6 depicts the comparison of the predicted and measured T3 temperatures for the battery under four thermal management modes at 1C, 1.5C and 2C discharge rates. The following observations can be made: 1) In comparison with other cooling methods, the rate of temperature rise with PCM-fin structure is the slowest for the same discharge rate. Further examination of Fig.6 also showed that the temperature rise of the battery is quickly suppressed at the early stage of the discharge process; and the thermal performance is excellent during the subsequent discharge process. Such result demonstrates the efficiency of PCM-fin structure in controlling the temperature of battery. 2) For the final temperature rise of each discharge process, the one with PCM-fin structure demonstrates its superiority over that with the other three cooling methods in the effectiveness of heat dissipation, especially a significant temperature drop of about 60% comparing to natural convection cooling at different discharge rates. 3) The predicted values of the temperature and its change trends under different conditions are in very good agreement with the measurements, demonstrating the accuracy and reliability of the current numerical model and its capacity to be used to assist the design of cooling techniques for battery thermal management.

These results demonstrated that the PCM-fin structure provided effect cooling to control the temperature rise of LIB during discharge, and has great potential to be exploited for practical applications.

3.2. Effect of PCM under different melting temperature

The appropriate phase change temperature is essential for improving the efficiency of battery cooling during discharge process. In this section, PCM44, PCM50 and PCM54 were compared in terms of their performance in controlling the battery temperatures. The physical properties of these three PCMs were listed in Table 1. The thickness of PCMs between each battery was set as 10mm, and the initial temperature of battery module was 40℃. Figure 7 shows the temperature contours of the four cases (without PCM, PCM54, PCM50 and PCM44) at the end of the 3C discharge under natural convection. The temperature of the case without PCM was much higher than the other cases, and all cases with PCM demonstrated obvious reduction of heat accumulation due to the latent heat. Among them, PCM44 alleviated the heat accumulation of module more efficiently than PCM54 and PCM50. These results seem to indicate that the latent heat of PCM 44 is exploited more than other two PCMs due to its low melting temperature.

To further facilitate the comparison, the maximum temperature (T_{max}) on battery surface within the module at each case were extracted as shown in Figure 8. It can be seen that T_{max} of module without PCM was up to 68.6℃. However, T_{max} for PCM54, PCM50 and PCM44 were 62.8℃, 60.5℃ and 57.2℃, which were 5.8℃, 8.1℃ and 11.4℃ lower than that without PCM, respectively. In order to understand this phenomenon, the liquid factions of PCMs during the 3C discharge process were also presented in Fig. 8. It can be found that the onset time of phase change for PCM44, PCM50 or PCM54 was 169s, 575s or 839s, respectively. The onset time of phase change for PCM44 was much earlier than that of other two PCMs, which means the longer time to exploit the latent heat of PCM during the whole discharge process. The liquid fractions of PCM 44, PCM 50 and PCM 54 in the end of discharge process was 43.34%, 20.53% and 22.75%, which further indicate that the latent heat of other two PCMs is much less exploited than PCM 44. It means that PCM44 exhibits better performance as compared to PCM50 and PCM54 in reducing the module temperature, which can be ascribed to the lowest phase change temperature. From these effects, PCM44 was employed in following simulations.

Figure 9 shows the evolution of T_{max} and the minimum temperature (T_{min}) on battery surface within the module and the corresponding temperature change rates for the case of PCM44. From the dotted curves, it is found that the maximum temperature change rates appeared at the early stage of discharge process, whose time point was defined as Point A. Then, the temperature change rates

gradually decreased with the evolution of discharging until reaching the time of the minimum temperature rates as Point B. After a period of the plateau, the temperature change rates increased again, whose time point was defined as Point C. Therefore, the three points divided the whole discharge process into four segments. In the first segment, a rapid rise of T_{max} from 40℃ to 43℃ which is minimum temperature of phase transition was observed, as shown in Fig. 9(a). In this segment, heat conduction is the main manner of heat dissipation through PCM. As a result, heat generated from battery accumulates quickly leading to the faster temperature ramp-up rate.

Figure 10 demonstrates the computed liquid fraction of PCM layers in the middle cross section of battery module (as shown in Fig. 9(b)) corresponding to the Point A, B, C and the end time of discharge. From the Fig. 10(a), no phase change was found in the layer of PCM, which verifies the above deduction. In the AB segment, the temperature rate of T_{max} was slow down in Fig. 9(a). The main reason is the PCM adjacent to the upper surface of the batteries started to absorb the heat flux as latent heat of fusion, and the phenomenon was visualized in the liquid fraction of Point B in Fig. 10(b). With the increasing area of PCM adjacent to the battery surface was exploited, a stage of T_{max} growing linearly was observed during BC segment. It demonstrates that the rate of PCM storing thermal energy during this segment is fastest in the whole discharge process. As shown in Fig. 10(c), the PCM adjacent to battery surface was completely melted in the end of BC segment, which means the heat has to pass through liquid PCM to deeper layer of PCM. In the final segment, heat accumulation quickly occurred at the surface of batteries triggering the rate of T_{max} rising again owing to the limited convection magnitude of liquid PCM. Compared with Point C, the liquid fraction of end time shown in Fig. 10(d) was not obviously discrepant except the width of liquid PCM. From these results, it implies that lot of PCM in central section is not fully exploited due to its low thermal conductivity.

3.3. Effect of fin thickness and spacing

PCM-fin structure can effectively increase the heat exchange area of PCM to effectively enhance the heat transfer in the PCM. In this section, the design of fin structure including fin thickness (l) and fin spacing (d) was investigated to find the best dimension to restrain the temperature rise of cells. Fin thickness (l) was set as 0.5mm, 1mm, 1.5mm and 2mm respectively, and fin spacing (d) was constant as 2.5mm. Figure 11 shows the temperature contours of the battery module with different fin thicknesses at the end of 3C discharge. For the case of pure PCM, the temperature in the central layer

of PCM was basically approaching to 40℃, which was minimum in all cases. Whereas the batteries still presented high temperature. Compared to this case, other cases with fins got the better temperature performance for the batteries with the function of utilizing the latent heat in central section of PCM layer.

Figure 12(a) demonstrates the distribution of T_{max} in the battery module under different fin thicknesses at the end of 3C discharge, and Fig. 12(b) shows the maximum temperature of tabs and the temperature difference (ΔT) of battery module. Apparently, the maximum temperature of tabs and the ΔT both were beyond the specified range in the case of l = 2 mm, which could result in significant capacity loss of battery. With the decrease of fin thickness, T_{max}, ΔT and the maximum temperature of tabs decreased, specially ΔT and the maximum temperature of tabs were well controlled under 5℃ and 60℃, when k was 1mm or 0.5mm. These results illustrate that although thicker fin can enhance thermal conduction, the increasing fin thickness inevitably leads to a decrease in the volume of PCM within a heat sink of fixed width and thickness. Consequently, it results in a corresponding reduction in the amount of heat that the PCM can absorb. When the fin spacing is constant, the smaller fin thickness, the more number of fins than the thicker fin could increase the heat exchange area with PCM, thus the performance of heat dissipation is improved. As shown in Fig. 12(a), it was observed that the temperature distribution was inconsistent in every case, which presented the situation of high temperature appearing in the edge of battery module and low temperature emerging at the middle part. It is caused by the arrangement of the heat sinks, as shown in Fig. 1, cells in edge of battery module were only equipped with heat sink with fin on one side, while the middle cells contacted with heat sinks on both sides.

In PCM-fin structure, the fin spacing (d) is another important factor. Six types of fin spacing, which changed from 1mm to 3.5mm and l=0.5mm was chosen to study the influence on the fin spacing. As listed in Table 7, it can be seen that the decrease of fin spacing leads to the increase of fin number and heat dissipation ratio, which reduces the volume fraction of PCM accordingly. The heat dissipation ratio in this work was defined by the ratio of the heat exchange area of the baseboard with fin structure to that of the baseboard without fin.

Figure 13(a) displays the distribution of T_{max} in the battery module under different fin spacing at

the end of 3C discharge, and Fig. 13(b) illustrates the maximum temperature of tabs and the temperature difference (ΔT) of battery module. It can be seen that the change of temperature distribution with the decrease of fin spacing was nonlinear. At first, T_{max}, ΔT and the maximum temperature of tabs reduced gradually with the decrease of fin spacing from 3.5mm to 2.5mm. It is because that the latent heat of PCM can be better utilized due to the reduction of fin spacing improving the heat exchange area with PCM, while the volume fraction of PCM has little effect from 88.1% to 84% in this segment as shown in Table 7. Nonetheless, the maximum temperature of tabs, T_{max} and ΔT began to increase as the fin spacing continued to decrease from 2.5mm to 1mm, which also means the fin number further increasing. Although the increased fin numbers lead to the increase of the heat transfer area, it also causes the excessive reduction of the volume of PCM. As shown in Table 7, the volume fraction of PCM decreased from 84% to 67.26% in this segment. Meanwhile, the liquid fraction of PCM rapidly increased at the end of discharge because of the reduction in latent heat of PCM. It reveals that the negative influence of decreasing volume of PCM is more significant than the positive effect of increasing the heat transfer area on thermal performance of the module. Therefore, the results demonstrate that the configuration with the fin spacing of 2.5mm has more advantage in controlling the temperature rise of the battery module than other cases. In contrast, the performance of heat dissipation in the case with d=2.5mm is better than d=2mm, and it also reduces the difficulty of manufacturing process compared to the cases with 2mm.

3.4. Effect of PCM thickness

The PCM was set between the fins whose thickness determines the space between adjacent batteries, and also influences the energy density of module. In this section, the effect of different PCM thickness were investigated. The influence of PCM thicknesses with 6mm, 8mm, 10mm, 12mm and 14mm were simulated. Figure 14 illustrates the temperature contours of battery module with different PCM thicknesses at the end of 3C discharge. Apparently, with the augment of PCM thickness from 6mm to 10mm, the temperature distribution was remarkably improved.

Figure 15(a) shows the maximum temperature of tabs under different PCM thicknesses at the end of 3C discharge. Fig. 15(b) shows the temperature difference (ΔT) of battery module and the PCM liquid fraction at the end of 3C discharge. When the thickness was 6 mm, the maximum temperature

of tabs was 62.18℃ and the temperature difference of battery module was 6.55℃, which were both exceed the desired range.

Fig. 15(b) shows that the PCM liquid fraction in *h*=6mm was nearly 100%, which means that the PCM has completely melted in the final stage of discharge. It indicates that in this case, a rapid accumulation of heat in the later period and rapid temperature rise of the battery occurred. Therefore, the PCM with the thickness of 6 mm is not sufficient for controlling the temperature rise of the battery. As the PCM thickness increased to 8 mm, the maximum temperature of tabs and the temperature difference of battery module were also not in the desired temperature range, although the temperature distribution was much better than the case of *h*=6 mm.

For the case of *h*=10mm, the maximum temperature of the tabs decreased to 59.06℃, and the temperature difference was limited in 4.7℃, which means *h*=10mm can maintain the suitable temperature performance. However, when the thickness further increased, the temperature distribution reduced at a lower rate as shown in Fig. 14. Moreover, the maximum temperature of tabs and the temperature difference of battery module were only decreased by 0.73℃ and 0.37℃ at the thickness between 10mm and 14mm, as shown in Fig. 15. Such results imply that although the thicker PCM can lead a lower temperature and temperature differences of batteries, the effect of the thicker PCM than 10 mm in this study is minor. In addition, the thicker the PCM is, the heavier and more complex the structure of heat sink is, as well as higher cost in the practical applications. Consequently, these results imply that a PCM thickness of 10mm is enough in this study.

3.5. Comparison on thermal behavior of pure PCM and PCM-fin structure

In comparison with pure PCM, PCM-fin structure can enhance the heat exchange area of PCM by uniformly allocating straight fins into PCM, but it will decrease the volume of PCM between two baseplates. In this section, the thermal behaviors of pure PCM and PCM-fin structure within the module during discharge were analyzed and compared to further confirm the effect of fins structure on thermal performance. Figure 16(a) demonstrates the evolution of T_{max} and PCM liquid fraction under the cases of pure PCM and PCM-fin structure during 3C discharge. It is observed that T_{max} of PCM-fin structure was greatly reduced by attaching fins, while the liquid fraction of PCM eventually was 72.37%, nearly twice the value of the pure PCM case at the end of discharging. By examining the representative time points as described in Section 3.2, Point A, B, and C were identified in the curve

of T_{max} for the case of PCM-fin structure. It can be found that the time to reach Point A was the same in both cases as shown in Fig. 16(a). The reason lies in that the edge of PCM layer contacting with the aluminum baseplate firstly absorbed heat released by the batteries in the initial stage of discharge, such process is independent of the fin structure.

Figure 17 shows the computed liquid fraction of PCM layers in the middle cross section of battery module (as shown in Fig. 16(b)) corresponding to Point A, B, C and end time in the case of PCM-fin structure. The liquid fraction can be found as nearly zero at Point A as shown in Fig 17(a), which was the same as the case of pure PCM. However, as T_{max} continued to exceed the minimum temperature of phase transition, the case of PCM-fin structure reduced the battery temperature ramp-up rate at the same discharge condition. The time of Point B was also advanced comparing to the pure PCM case. The reason is that the heat can be timely transferred into the deeper layers of PCM through the conduction of fins. Therefore, it is clearly seen that the upper layer of PCM almost started to phase change as shown in Fig. 17(b), while the phenomenon was only observed on the upper edge of PCM in the case of pure PCM due to the low thermal conductivity.

The BC segment in which T_{max} grew linearly was almost forming the temperature plateau in the case of PCM-fin structure, whose temperature rise was merely 1.3℃. A study by Eftekhar et al. [55] explains that natural convection is the dominant mode of heat transfer during the PCM melting process, and fin induces a naturally buoyant flow in their neighborhood causing rapid melting of the PCM. As a result, most of latent heat in the upper layer of PCM was exploited while the lower half of the PCM layer just began to undergo phase transition, as shown in Fig. 17(c). What's more, the work time of BC segment was also prolonged. Figure 17(d) indicates that the heat released by the batteries can be absorbed by the whole layers of PCM during the discharge, and the availability of latent heat is great augmented, when the exchange heat area is increased by the fins. Although the introduction of fins slightly reduces the PCM volume, the fins influence the thermal behavior of PCM due to improved heat conduction and natural convection. In particular, PCM-fin structure further enhanced the thermal performance of the battery module by restraining the temperature rise in the mid-late discharging process. The final PCM liquid fraction achieved to 72.37% and was much higher than that of the pure PCM case, which was 43.32%. It demonstrates that PCM-fin structure can significantly improve the thermal performance of battery.

3.6. Cycle test

Under continuous cycles, the heat accumulated during cycling might not be effectively dissipated arising from the limitation of heat transfer between PCMs and ambient, and consequently leads to potential failures of BTM using PCMs. In order to investigate the thermal performance of the as-designed PCM-fin structure in a practical application, the battery modules equipped with pure PCM, PCM/EG and PCM-fin, respectively, were simulated under 5 continuous cycles. All PCM was n-docosane and the ambient temperature was 40℃. To conduct a fairer comparison, the parameters in the PCM/EG system were presented by Sarı et al. [56], whose work also chose n-docosane as experimental PCM. It is important to note that the melting temperature of PCM/EG was 43℃ which was lower than that of pure PCM as 1℃. Figure 18 shows a charging and discharging pattern with rates of 0.5C and 2C, respectively.

Figure 19 shows the variations of T_{max} and liquid fraction with time for cycle test under different BTMs. Figure 19(a) shows that the maximum temperature of each cycle for pure PCM system increased gradually, and the temperature exceeded 50℃ in the final two discharge process. Although the temperature rise was lower than pure PCM system in early stage of cycling, PCM/EG system presented much bigger amplitude of temperature variation. PCM/EG system underwent a higher temperature rise after the third cycle. For the PCM-fin system, a stable temperature profile after the first cycle was obtained and then the initial temperature and T_{max} stayed at about 43℃ and 48℃ in each cycle.

As shown in Fig. 19(b), the degree of phase change in PCM/EG system was higher than other systems after the first discharge due to the lower melting temperature and high thermal conductivity. This contributes a better performance on controlling the temperature rise than pure PCM system in the early stage of cycling. Nonetheless, the heat transfer efficiency between PCM/EG and the ambient was not able to dissipate promptly the absorbed heat from PCM to ambient during the following charge and rest time. As a result, the initial liquid fraction of PCM/EG system was 31.9% and 60.2% at the second and third discharge, respectively. This means almost all latent heat of PCM has already been exploited in the third cycle, which might lead to failure of BTM in the following cycles. Comparing with PCM/EG, pure PCM system has more PCM volume that means more latent heat can be utilized. However, the PCM liquid fraction was consistently below 100% during the cycles. The module in

pure PCM cannot meet the suitable temperature rising limits due to the low thermal conductivity.

The case of PCM-fin structure demonstrates not only much improved thermal performance during discharge process, but also significant effect on the solidification process during the charge and the rest period. The average declining liquid fraction during this period in each cycle was 34%, which was twice than that in case of pure PCM. It can be explained that conduction is the dominant mode of heat transfer during the solidification process of PCM, and the presence of fins enhances the heat transfer efficiency between PCM and ambient due to improved heat conduction and large heat transfer surface. In the field of latent heat thermal energy storage, the finding was also discovered in the study of Stritih et al. [36]. They found about 40% reduction in solidification time due to the presence of fins, and proposed that the optimizing effect of fins on solidification process is better than the melting process of PCM. These points prove that PCM-fin structure can improve thermal performance and prolong the duration of thermal control for the battery module under continue cycles by enhancing natural convection and heat conduction of PCM.

4. Conclusions

A novel PCM-fin structure based BTM system was proposed for a prismatic LFP battery module. A 1D-electrochemical and 3D-thermal coupled model for LFP/C battery module was firstly designed and the thermal contact resistance was considered between different materials during the heat transfer process. Four different cooling methods including air, fin, pure PCM and composite cooling for single LIB cell were investigated through carefully designed experiments, to verify the effectiveness of the composite design and the accuracy of the coupled model. In order to optimize the passive BTM system, a battery module with five cells was selected to study the influences of pure PCM under different melting temperature, fin thickness, fin spacing and PCM thickness on the thermal performance. Maximum temperature on battery surface and temperature difference within the battery module were monitored. Further numerical studies also were conducted involving 5 continuous charge-discharge cycles to study the effect of PCM-fin structure on endurance under the adverse conditions. The concluding remarks could be made as follow:

(1) PCM with lower melting temperature can improve the thermal performance of LIB, however the improvement is limited due to the relatively low thermal conductivity. Utilizing the PCM-fin structure could obtain the lowest temperature and the best temperature uniformity than other

cooling cases in this study owing to the increasing heat exchange area of PCM by fin.

(2) Decreasing fin thickness could reduce the maximum temperature and temperature difference of battery module by increasing the heat exchange area with PCM. The fin spacing is also an important factor, which should be carefully considered when designing the PCM-fin structure. Fins with excessively small spacing would contribute to the negative influence of decreasing the volume of PCM, which is more significant than the positive effect of increasing the heat transfer area.

(3) Increasing appropriately the PCM thickness could improve the thermal performance and is more efficient than other factors. After the PCM thickness exceeded the critical value of 10 mm, the enhancement of the heat dissipation efficiency was insignificant in the thermal management system investigated in this work.

(4) The latent heat of PCM can be fully utilized due to improved heat conduction and natural convection of the PCM-fin structure. Compared with pure PCM, PCM-fin structure with optimization design can increase the final PCM liquid fraction by 29.05%, and reduce the maximum surface temperature of battery module by 36.4%.

(5) In the cycle test, PCM-fin structure can decrease the solidification time of PCM during the heat dissipation period. As a result, it reduces the failure risk in passive thermal management systems using PCMs.

Acknowledgements

This work is supported by the National Natural Science Foundation of China (No. 51604297), the European Commission's Marie Curie Action, the Key Research and Development Program of Shandong Province (2018GSF120011), and Fundamental Research Funds for the Central Universities (No. 18CX07005A). Dr Ping is supported by the European Commission's Marie Curie Incoming International Fellowship grant (No. 656582).

References

[1] Global Electric Vehicle Market Outlook, 2018. Frost&Sullivan2018.
[2] L. Fusheng. New energy car sales to be 10% of total by 2020. China Daily2018.

[3] Nordic EV outlook 2018. International Energy Agency2018.
[4] K. Itani, A. De Bernardinis, Z. Khatir, A. Jammal. Comparative analysis of two hybrid energy storage systems used in a two front wheel driven electric vehicle during extreme start-up and regenerative braking operations. Energy Conversion and Management. 144 (2017) 69-87.
[5] M.I. Fahmi, R. Rajkumar, R. Arelhi, R. Rajkumar, D. Isa. The performance of a solar PV system using supercapacitor and varying loads. 2014 IEEE Student Conference on Research and Development2014. pp. 1-5.
[6] M.K. Döşoğlu. Nonlinear dynamic modeling for fault ride-through capability of DFIG-based wind farm. Nonlinear Dynamics. 89 (2017) 2683-94.
[7] K. Ghedamsi, D. Aouzellag, E.M. Berkouk. Control of wind generator associated to a flywheel energy storage system. Renewable Energy. 33 (2008) 2145-56.
[8] L. Qu, W. Qiao. Constant Power Control of DFIG Wind Turbines With Supercapacitor Energy Storage. IEEE Transactions on Industry Applications. 47 (2011) 359-67.
[9] N. Mendis, K.M. Muttaqi, S. Perera. Active power management of a super capacitor-battery hybrid energy storage system for standalone operation of DFIG based wind turbines. 2012 IEEE Industry Applications Society Annual Meeting2012. pp. 1-8.
[10] M. Kenan Döşoğlu, A.B. Arsoy. Transient modeling and analysis of a DFIG based wind farm with supercapacitor energy storage. International Journal of Electrical Power & Energy Systems. 78 (2016) 414-21.
[11] J. Sun, J. Li, T. Zhou, K. Yang, S. Wei, N. Tang, et al. Toxicity, a serious concern of thermal runaway from commercial Li-ion battery. Nano Energy. 27 (2016) 313-9.
[12] Y. Chung, W. Jhang, W. Chen,Y. Wang, C. Shu. Thermal hazard assessment for three C rates for a Li-polymer battery by using vent sizing package 2. Journal of Thermal Analysis and Calorimetry 127 (2017) 809-817.
[13] R. German, P. Delarue, A. Bouscayrol. Battery Pack Self-heating During the Charging Process. 2018 IEEE International Conference on Industrial Technology (ICIT), 70 (2018) 2049-2054.
[14] A. Väyrynen, J. Salminen. Lithium ion battery production. The Journal of Chemical Thermodynamics. 46 (2012) 80-5.
[15] N. Yang, X. Zhang, B. Shang, G. Li. Unbalanced discharging and aging due to temperature differences among the cells in a lithium-ion battery pack with parallel combination. Journal of Power Sources. 306 (2016) 733-41.
[16] A.A. Pesaran. Battery thermal models for hybrid vehicle simulations. Journal of Power Sources. 110 (2002) 377-82.
[17] S.K. Mohammadian, Y. Zhang. Thermal management optimization of an air-cooled Li-ion battery module using pin-fin heat sinks for hybrid electric vehicles. Journal of Power Sources. 273 (2015) 431-9.
[18] S. Hong, X. Zhang, K. Chen, S. Wang. Design of flow configuration for parallel air-cooled battery thermal management system with secondary vent. International Journal of Heat and Mass Transfer. 116 (2018) 1204-12.
[19] T. Wang, K.J. Tseng, J. Zhao. Development of efficient air-cooling strategies for lithium-ion battery module based on empirical heat source model. Applied Thermal Engineering. 90 (2015) 521-9.
[20] J. Zhao, Z. Rao, Y. Li. Thermal performance of mini-channel liquid cooled cylinder based battery thermal management for cylindrical lithium-ion power battery. Energy Conversion and Management. 103 (2015) 157-65.
[21] Z. Qian, Y. Li, Z. Rao. Thermal performance of lithium-ion battery thermal management system by using mini-channel cooling. Energy Conversion and Management. 126 (2016) 622-31.
[22] Y. Ren, Z. Yu, G. Song. Thermal management of a Li-ion battery pack employing water evaporation. Journal of Power Sources. 360 (2017) 166-71.
[23] R. Sabbah, R. Kizilel, J.R. Selman, S. Al-Hallaj. Active (air-cooled) vs. passive (phase change material) thermal management of high power lithium-ion packs: Limitation of temperature rise and uniformity

of temperature distribution. Journal of Power Sources. 182 (2008) 630-8.
[24] S. Al-Hallaj, J. Selman. A Novel Thermal Management System for Electric Vehicle Batteries Using Phase-Change Material2000.
[25] C. Lin, S. Xu, G. Chang, J. Liu. Experiment and simulation of a LiFePO4 battery pack with a passive thermal management system using composite phase change material and graphite sheets. Journal of Power Sources. 275 (2015) 742-9.
[26] Y. Xie, J. Tang, S. Shi, Y. Xing, H. Wu, Z. Hu, et al. Experimental and numerical investigation on integrated thermal management for lithium-ion battery pack with composite phase change materials. Energy Conversion and Management. 154 (2017) 562-75.
[27] F. Samimi, A. Babapoor, M. Azizi, G. Karimi. Thermal management analysis of a Li-ion battery cell using phase change material loaded with carbon fibers. Energy. 96 (2016) 355-71.
[28] J. Yan, K. Li, H. Chen, Q. Wang, J. Sun. Experimental study on the application of phase change material in the dynamic cycling of battery pack system. Energy Conversion and Management. 128 (2016) 12-9.
[29] S.A. Khateeb, S. Amiruddin, M. Farid, J.R. Selman, S. Al-Hallaj. Thermal management of Li-ion battery with phase change material for electric scooters: experimental validation. Journal of Power Sources. 142 (2005) 345-53.
[30] G. Jiang, J. Huang, Y. Fu, M. Cao, M. Liu. Thermal optimization of composite phase change material/expanded graphite for Li-ion battery thermal management. Applied Thermal Engineering. 108 (2016) 1119-25.
[31] M.A. AlMaadeed, S. Labidi, I. Krupa, M. Karkri. Effect of expanded graphite on the phase change materials of high density polyethylene/wax blends. Thermochimica Acta. 600 (2015) 35-44.
[32] A. Alrashdan, A.T. Mayyas, S. Al-Hallaj. Thermo-mechanical behaviors of the expanded graphite-phase change material matrix used for thermal management of Li-ion battery packs. Journal of Materials Processing Technology. 210 (2010) 174-9.
[33] R. Pakrouh, M.J. Hosseini, A.A. Ranjbar, R. Bahrampoury. A numerical method for PCM-based pin fin heat sinks optimization. Energy Conversion and Management. 103 (2015) 542-52.
[34] A. Castell, C. Solé, M. Medrano, J. Roca, L.F. Cabeza, D. García. Natural convection heat transfer coefficients in phase change material (PCM) modules with external vertical fins. Applied Thermal Engineering. 28 (2008) 1676-86.
[35] Z. Khan, Z. Khan, A. Ghafoor. A review of performance enhancement of PCM based latent heat storage system within the context of materials, thermal stability and compatibility. Energy Conversion and Management. 115 (2016) 132-58.
[36] U. Stritih. An experimental study of enhanced heat transfer in rectangular PCM thermal storage. International Journal of Heat and Mass Transfer. 47 (2004) 2841-7.
[37] S. Mat, A.A. Al-Abidi, K. Sopian, M.Y. Sulaiman, A.T. Mohammad. Enhance heat transfer for PCM melting in triplex tube with internal–external fins. Energy Conversion and Management. 74 (2013) 223-36.
[38] L. Yang, H. Peng, X. Ling, H. Dong. Numerical analysis on performance of naphthalene phase change thermal storage system in aluminum plate-fin unit. Heat and Mass Transfer. 51 (2014) 195-207.
[39] Z. Liu, X. Sun, C. Ma. Experimental investigations on the characteristics of melting processes of stearic acid in an annulus and its thermal conductivity enhancement by fins. Energy Conversion and Management. 46 (2005) 959-69.
[40] A.A. Al-Abidi, S. Mat, K. Sopian, M.Y. Sulaiman, A.T. Mohammad. Internal and external fin heat transfer enhancement technique for latent heat thermal energy storage in triplex tube heat exchangers. Applied Thermal Engineering. 53 (2013) 147-56.
[41] S. Mahmoud, A. Tang, C. Toh, R. Al-Dadah, S.L. Soo. Experimental investigation of inserts configurations and PCM type on the thermal performance of PCM based heat sinks. Applied Energy. 112 (2013) 1349-56.
[42] Z. Wang, H. Zhang, X. Xia. Experimental investigation on the thermal behavior of cylindrical battery

with composite paraffin and fin structure. International Journal of Heat and Mass Transfer. 109 (2017) 958-70.
[43] S. Himran, A. Suwono, G.A. Mansoori. Characterization of Alkanes and Paraffin Waxes for Application as Phase Change Energy Storage Medium. Energy Sources. 16 (1994) 117-28.
[44] R. Zhao, J. Gu, J. Liu. Optimization of a phase change material based internal cooling system for cylindrical Li-ion battery pack and a hybrid cooling design. Energy. 135 (2017) 811-22.
[45] K. Pielichowska, K. Pielichowski. Phase change materials for thermal energy storage. Progress in Materials Science. 65 (2014) 67-123.
[46] H. Liu, Z. Wei, W. He, J. Zhao. Thermal issues about Li-ion batteries and recent progress in battery thermal management systems: A review. Energy Conversion and Management. 150 (2017) 304-30.
[47] M. Doyle, T.F. Fuller, J. S. Newman. Modeling of Galvanostatic Charge and Discharge of the Lithium/Polymer/Insertion Cell1993.
[48] K. Li, J. Yan, H. Chen, Q. Wang. Water cooling based strategy for lithium ion battery pack dynamic cycling for thermal management system. Applied Thermal Engineering. 132 (2018) 575-85.
[49] S. Du, M. Jia, Y. Cheng, Y. Tang, H. Zhang, L. Ai, et al. Study on the thermal behaviors of power lithium iron phosphate (LFP) aluminum-laminated battery with different tab configurations. International Journal of Thermal Sciences. 89 (2015) 327-36.
[50] M. Xu, Z. Zhang, X. Wang, L. Jia, L. Yang. A pseudo three-dimensional electrochemical–thermal model of a prismatic LiFePO4 battery during discharge process. Energy. 80 (2015) 303-17.
[51] M. Bahrami, R. Culham, M. Yovanovich. Thermal resistances of gaseous gap for conforming rough contacts. 42nd AIAA Aerospace Sciences Meeting and Exhibit2004. p. 821.
[52] M. Grujicic, C.L. Zhao, E.C. Dusel. The effect of thermal contact resistance on heat management in the electronic packaging. Applied Surface Science. 246 (2005) 290-302.
[53] J. Holman. Heat Transfer 8th edition, MaGraw-Hill. Inc New York. (1997).
[54] P. Huang, A. Verma, D.J. Robles, Q. Wang, P. Mukherjee, J. Sun. Probing the cooling effectiveness of phase change materials on lithium-ion battery thermal response under overcharge condition. Applied Thermal Engineering. 132 (2018) 521-30.
[55] J. Eftekhar, A. Haji-Sheikh, D.Y.S. Lou. Heat Transfer Enhancement in a Paraffin Wax Thermal Storage System. Journal of Solar Energy Engineering. 106 (1984) 299-306.
[56] A. Sarı, A. Karaipekli. Thermal conductivity and latent heat thermal energy storage characteristics of paraffin/expanded graphite composite as phase change material. Applied Thermal Engineering. 27 (2007) 1271-7.

Table 1 Specifications and parameters of LFP battery and aluminum materials.

Parameter	Value
Capacity (Ah)	10
Mass of cell (g)	235
Voltage (V)	3.2
Internal resistance (mΩ)	6
Width of cell (mm)	82
Thickness of cell (mm)	11
Height of cell (mm)	138
Specific heat of aluminum (J kg^{-1} K^{-1})	900
Thermal conductivity of aluminum (W m^{-1} K^{-1})	201
Density of aluminum (kg m^{-3})	2700

Table 2 Physical properties of paraffin wax (n-docosane, n-tetracosane, n-pentacosane) [43-45].

Property	n-docosane	n-tetracosane	n-pentacosane
Melting temperature (°C)	44	50	54
Melting range (°C)	2	2	3
Latent heat (kJ kg^{-1})	249	255	235
Specific heat, solid (J kg^{-1} K^{-1})	2150	2148	2150
Specific heat, liquid (J kg^{-1} K^{-1})	2275	2273	2180
Thermal conductivity, solid (W m^{-1} K^{-1})	0.21	0.21	0.21
Thermal conductivity, liquid (W m^{-1} K^{-1})	0.15	0.15	0.152
Density, solid (kg m^{-3})	791	796	814
Density, liquid (kg m^{-3})	771	770	724

Table 3 Governing equations of thermal-electrochemical model [47, 48].

Physical mechanism	Equations
Mass conservation of Li^+ species	
Solid phase	$\frac{\partial c_s}{\partial t} = \frac{D_s}{r^2}\frac{\partial}{\partial r}\left(r^2\frac{\partial c_s}{\partial r}\right)$
Boundary conditions	$D_s\frac{\partial c_s}{\partial r}\Big\|_{r=0} = 0, D_s\frac{\partial c_s}{\partial r}\Big\|_{r=R_c} = J$
Electrolyte phase	$\varepsilon_e\frac{\partial c_e}{\partial t} = \frac{\partial}{\partial x}\left(D_e\frac{\partial c_e}{\partial x}\right) + \left(1-t_+^0\right)a_s J$
Boundary conditions	$D_l^{eff}\frac{\partial c_e}{\partial x}\Big\|_{x=0} = D_l^{eff}\frac{\partial c_e}{\partial x}\Big\|_{x=L_{pos\_cc}+L_{pos}+L_{sep}+L_{neg}+L_{neg\_cc}} = 0$
Charge conservation	
Solid phase	$-K_s^{eff}\frac{\partial^2\varphi_s}{\partial x^2} = -a_s FJ$
Boundary conditions	$-K_s^{eff}\frac{\partial^2\varphi_s}{\partial x}\Big\|_{x=0} = -K_s^{eff}\frac{\partial\varphi_s}{\partial x}\Big\|_{x=L_{pos\_cc}+L_{pos}+L_{sep}+L_{neg}+L_{neg\_cc}} = \frac{I}{A}$
	$K_s^{eff}\frac{\partial\varphi_s}{\partial x}\Big\|_{x=L_{neg}+L_{neg\_cc}} = K_s^{eff}\frac{\partial\varphi_s}{\partial x}\Big\|_{x=L_{neg}+L_{neg\_cc}+L_{sep}} = 0$
	$\varphi_s\big\|_{x=0} = 0, \varphi_s\big\|_{x=L_{pos\_cc}+L_{pos}+L_{sep}+L_{neg}+L_{neg\_cc}} = E_{cell}$
Electrolyte phase	$-\frac{\partial}{\partial x}\left(\kappa^{eff}\frac{\partial\varphi_e}{\partial x}\right) + \frac{\partial}{\partial x}\left(\kappa_D^{eff}\frac{\partial}{\partial x}\ln c_e\right) = a_s FJ$
Boundary conditions	$\frac{\partial\varphi_e}{\partial x}\Big\|_{x=0} = \frac{\partial\varphi_e}{\partial x}\Big\|_{x=L_{pos\_cc}+L_{pos}+L_{sep}+L_{neg}+L_{neg\_cc}} = 0$
Butler-Volmer kinetics equation	
Exchange current density	$i_{0,i} = K_{0,i}\left(c_{2i,\max}\right)^{1-\beta}\left(c_{2i,\max}-c_{2i,surf}\right)^{1-\beta}\left(c_{2i,surf}\right)^{\beta}$
Over-potential	$\eta = \varphi_s - \varphi_e - E$
Energy conservation	
Heat transfer equation	$\rho_b C_{p,b}\frac{\partial T}{\partial t} = k_b\nabla^2 T + Q$
Boundary conditions	$Q_{conv} = h_c\left(T_s - T_\infty\right), Q_{rad} = h_r\sigma\left(T_s^4 - T_\infty^4\right)$
Thermal conductivity	$k_X = k_Z = \sum_i k_i L_i / \sum_i L_i, k_Y = \frac{\sum_i L_i}{\sum_i L_i / k_i}$
Internal generated heat	
Reversible heat	$Q_{rev} = -IT\left(\partial E_{OC}/\partial T\right) = -a_s JFT\left(\partial E_{OC}/\partial T\right)$
Irreversible heat	$Q_{rxn} = I\eta = a_s JF\left(E_{OC} - E\right)$
Internal heat-generation equation	$Q_{cell} = Q_{rev} + Q_{rxn}$

Table 4 Parameters used in the thermal-electrochemical model [49, 50].

Materials	Density ($kg\ m^{-3}$)	Specific heat ($J\ kg^{-1}\ K^{-1}$)	Thickness (mm)	Heat conductivity Coefficient ($J\ m^{-1}\ K^{-1}$)
LFP electrode	1500	1260.2	0.092	1.48
Graphite electrode	2660	1437.4	0.059	1.04
Separator	492	1978.16	0.02	0.334
Aluminum foil	2702	903	0.016	238
Copper foil	8933	385	0.009	398
Electrolyte	1290	133.9	--	0.45
Tab of negative electrode	2702	903	1	238
Tab of positive electrode	8933	385	1	398
Aluminum laminate film	1636	1376.947	1	0.427

Table 5 Governing equations of thermal contact resistance [52]

Subject equations	Explanations
The micro-contact resistance	
a single micro-contact resistance: $R_{s,i} = \frac{0.565 c_1 \left(\frac{\sigma}{m}\right)}{k_s P_f} \left(\frac{\sigma'}{m}\right)^{c_2}$	$\sigma = \sqrt{\sigma_1^2 + \sigma_2^2}, m = \sqrt{m_1^2 + m_2^2}, \quad \sigma' = \frac{\sigma}{\sigma_0}, k_s = \frac{2k_1 k_2}{k_1 + k_2}$
the overall micro-contact resistance: $R_s = \left(\sum_{i=1}^{n_s} \frac{1}{R_{s,i}} \right)^{-1}$	$n_s = \frac{1}{16} \left(\frac{m}{\sigma}\right)^2 \frac{\exp\left(-Y^2/\sigma^2\right)}{erf\left(Y/\sqrt{2}\sigma\right)} A_a$
The micro-gap thermal resistance	
$R_g = \frac{M + Y}{k_g A_a}$	$M = \left(\frac{2-\alpha_1}{\alpha_1} + \frac{2-\alpha_2}{\alpha_2}\right)\left(\frac{2\gamma}{1+\gamma}\right)\frac{1}{\Pr}\Lambda$, $\Lambda = C_\Lambda \frac{T_g}{P_g}, T_g = \frac{T_{cell} + T_i}{2}, Y = \sqrt{2}\sigma erfc^{-1}\left(\frac{2P}{H_{mic}}\right)$,
The overall thermal contact resistance	
$R_c = \left(\frac{1}{R_s} + \frac{1}{R_g} \right)^{-1}$	
Thermal contact conductivity	
$k_c = \frac{Y}{A_a R_c}$	

Table 6 Parameters used to compute the thermal contact resistance [52 54]

Parameter	Value
Battery-Al contact, RMS surface roughness, σ (um)	15
Al-PCM contact, RMS surface roughness, σ (um)	50
Al-Al contact, RMS surface roughness, σ (um)	2
The equivalent mean absolute surface slope, m	0.12
External pressure, P_f (kPa)	25
Vickers micro-hardness coefficient for aluminum, c_1 (GPa)	6.23
Vickers micro-hardness coefficient for aluminum, c_2	-0.23
Thermal accommodation coefficient, α	0.78
Specific heat ratio, γ	1.4
Prandtl number, Pr	0.69
Mean free path constant, C_Λ (m)	62.8×10^{-9}
Gas pressure, P_g (atm)	50
Thermal conductivity of gas, k_g (W m^{-1} K^{-1})	0.0299

Table 7 Summary of the fin structure data under different fin spacing.

Fin spacing (mm)	Fin number	Volume fraction of PCM	Heat dissipation area ratio	Final Liquid fraction
1	55	67.26%	7.33	90.06%
1.5	41	75.6%	5.75	83.05%
2	33	80.35%	4.86	77.21%
2.5	27	84%	4.17	72.37%
3	23	86.3%	3.71	70.01%
3.5	20	88.1%	3.375	68.42%

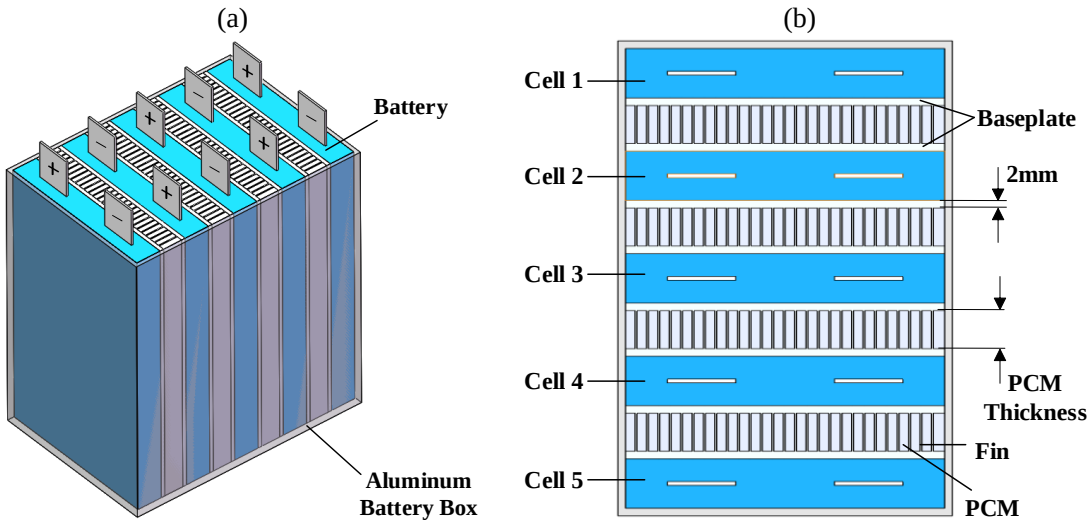

Fig. 1. Schematic of passive cooling system for the battery module: (a) side view, (b) top view.

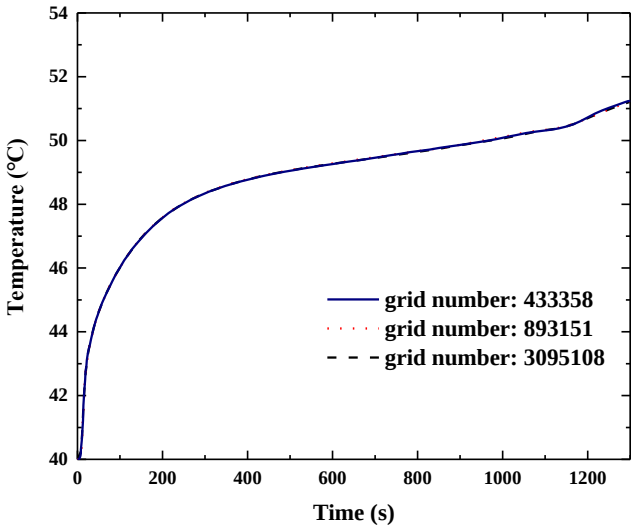

Fig. 2. Maximum temperature responses of the battery surface under the module with composite PCM-fin structure at different values of grid sizes.

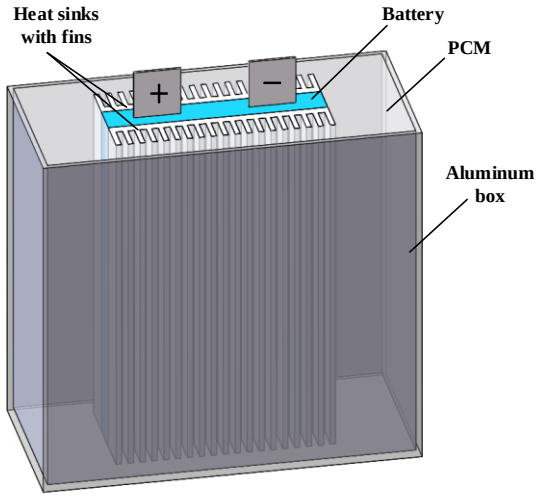

Fig. 3. Schematic diagram of single battery with PCM-fin structure.

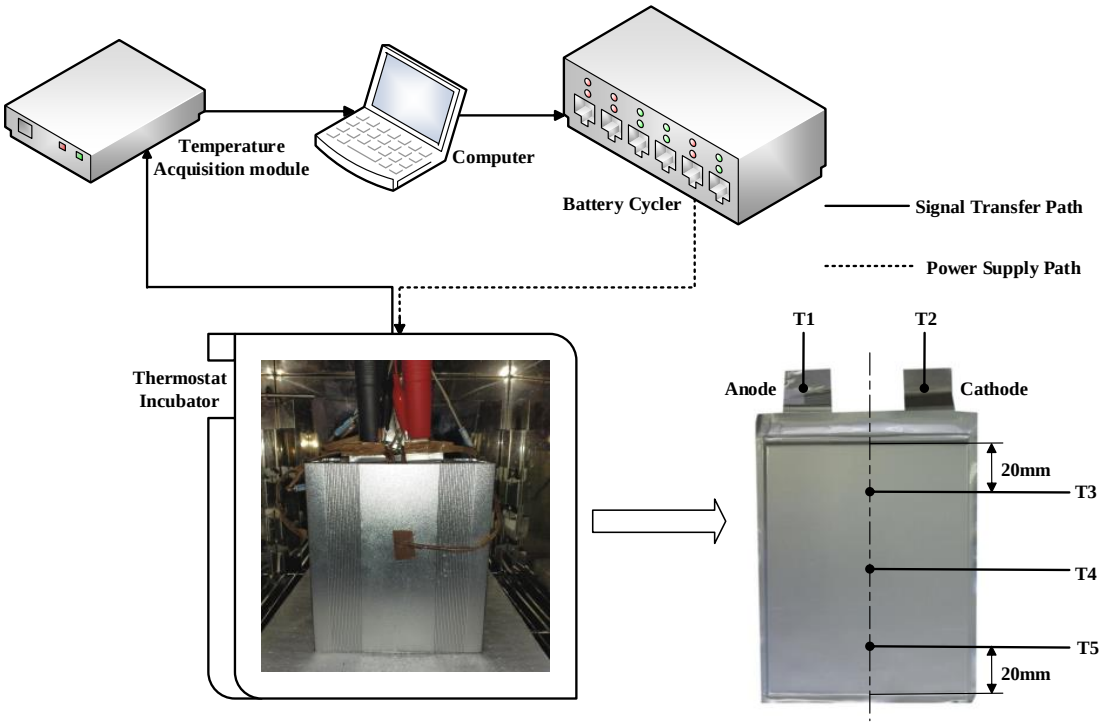

Fig. 4. Sketch of the experimental system and thermocouples locations in single battery.

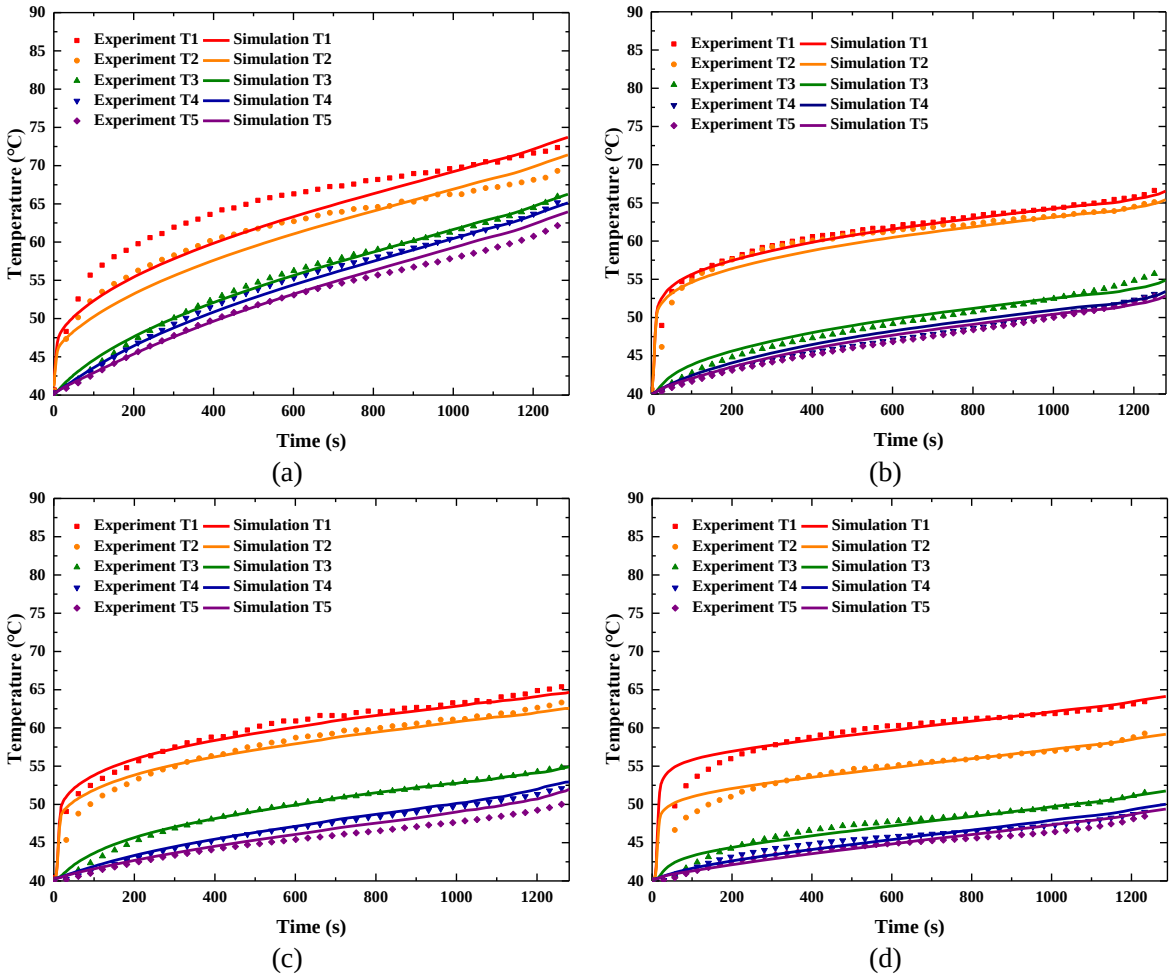

Fig. 5. Comparisons of the inhomogeneous temperature contours and evolution history obtained from prediction and measure during 3C discharge under different thermal management modes: (a) natural convection, (b) heat sink without PCM, (c) pure PCM and (d) PCM-fin structure.

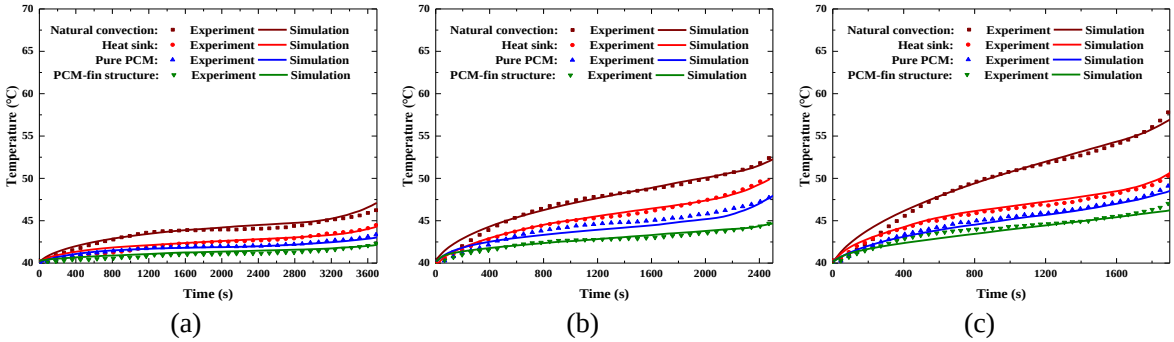

Figure. 6. Comparison of the predicted and measured T3 temperatures for the battery under four thermal management modes with different discharge rates: (a) 1C, (b) 1.5C and (c) 2C.

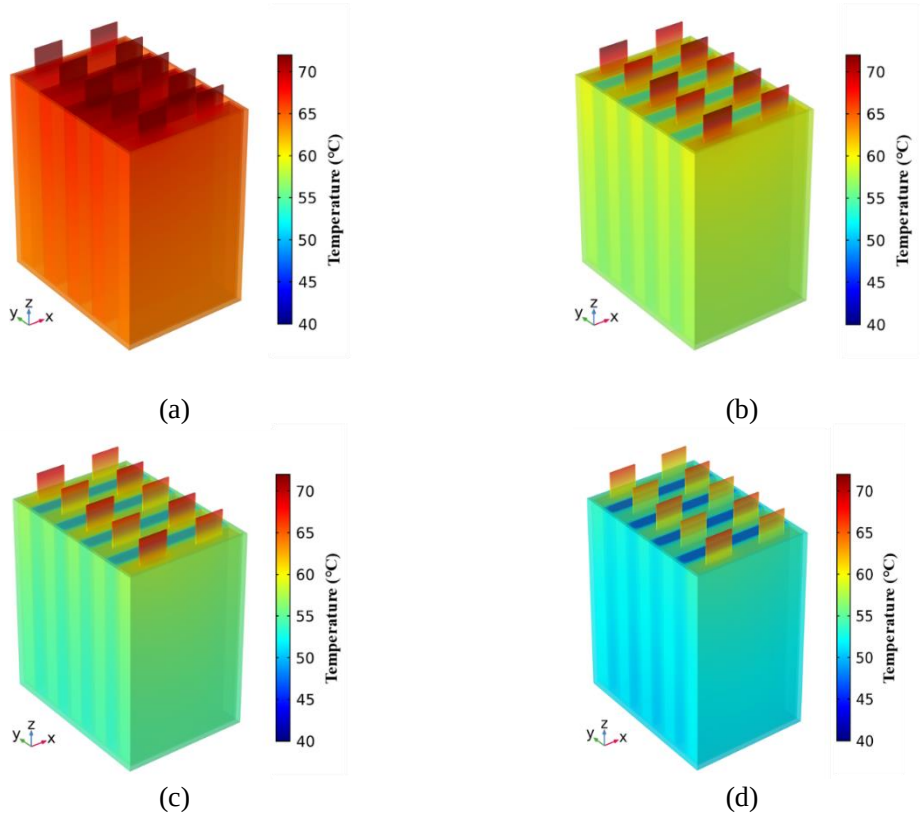

Fig. 7. Temperature contours of the four cases: (a) without PCM, (b) PCM54, (c) PCM50 and (d) PCM44, respectively, at the end of the 3C discharge under natural convection.

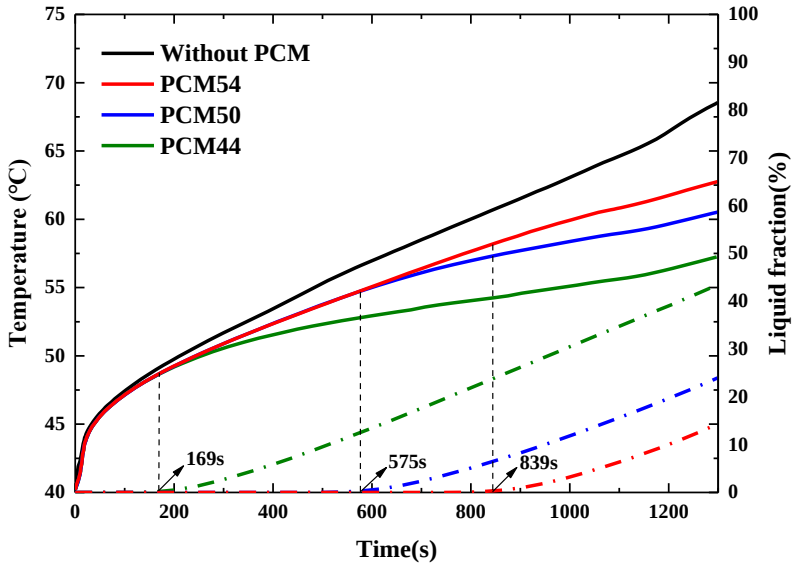

Fig. 8. Maximum temperature (T_{max}) on battery surface within the module and the liquid fraction of different PCMs during 3C discharge process.

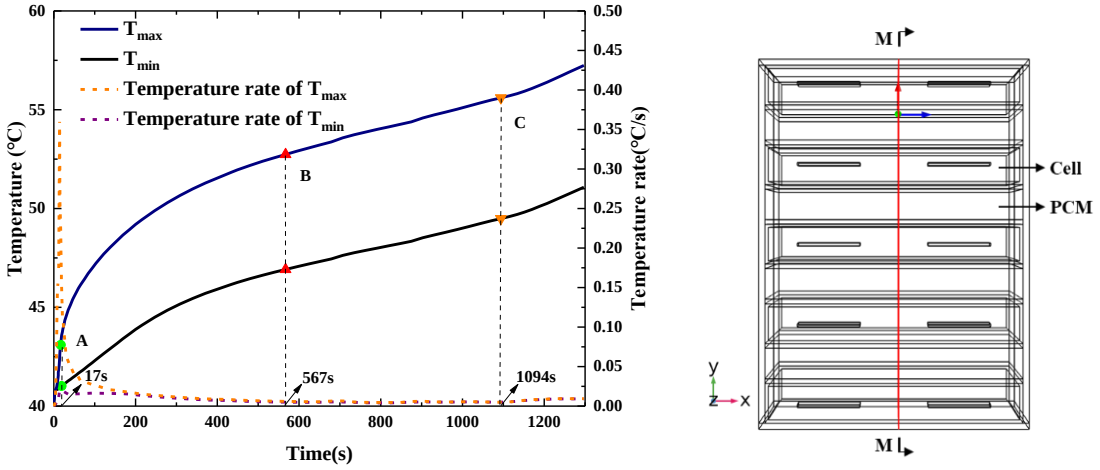

(a) (b)

Fig. 9. (a) Evolution of T_{max}, the minimum surface temperature of battery module (T_{min}) and the corresponding temperature rates under the case with PCM44. (b) Schematic of middle cross section (M-M) of battery module.

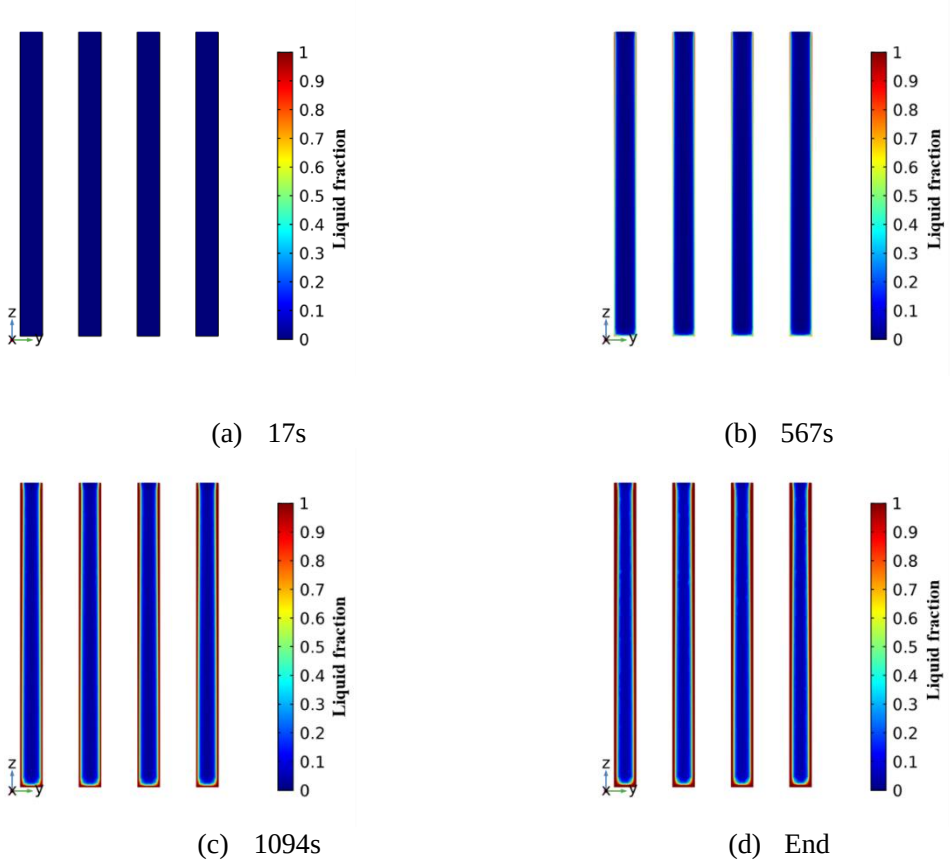

(a) 17s (b) 567s

(c) 1094s (d) End

Fig. 10. The computed liquid fraction in the middle cross section (M-M) of battery module for the pure PCM case at different time points A, B, C and end time.

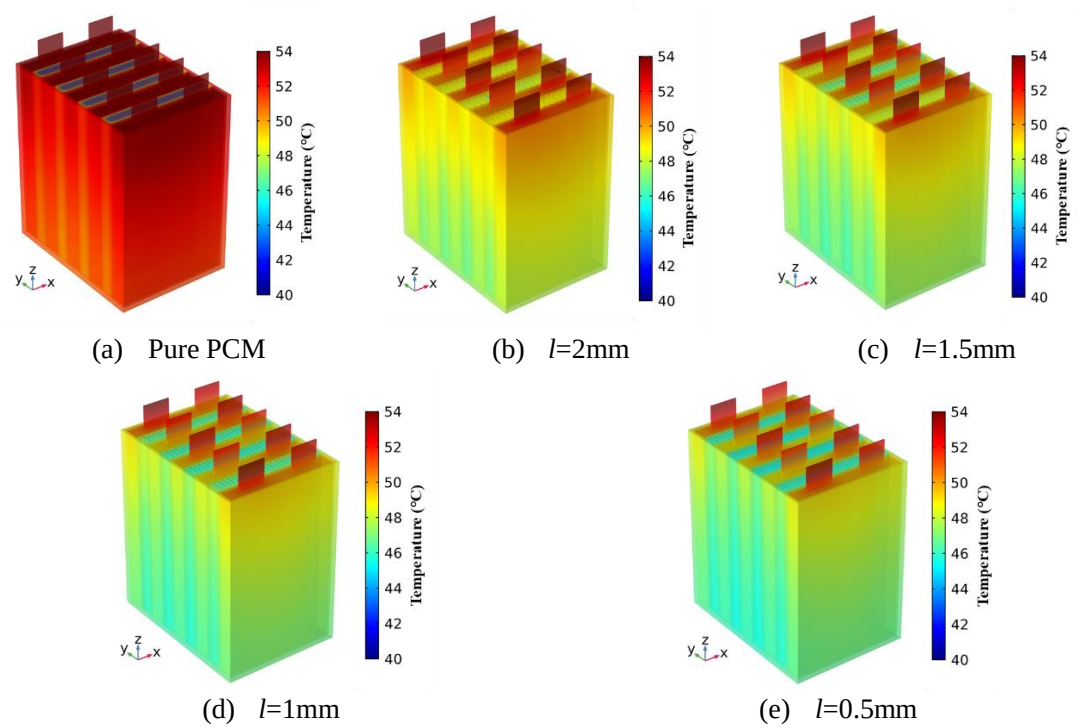

(a) Pure PCM (b) l=2mm (c) l=1.5mm

(d) l=1mm (e) l=0.5mm

Fig. 11. Temperature contours of the module with different fin thickness at the end of 3C discharge.

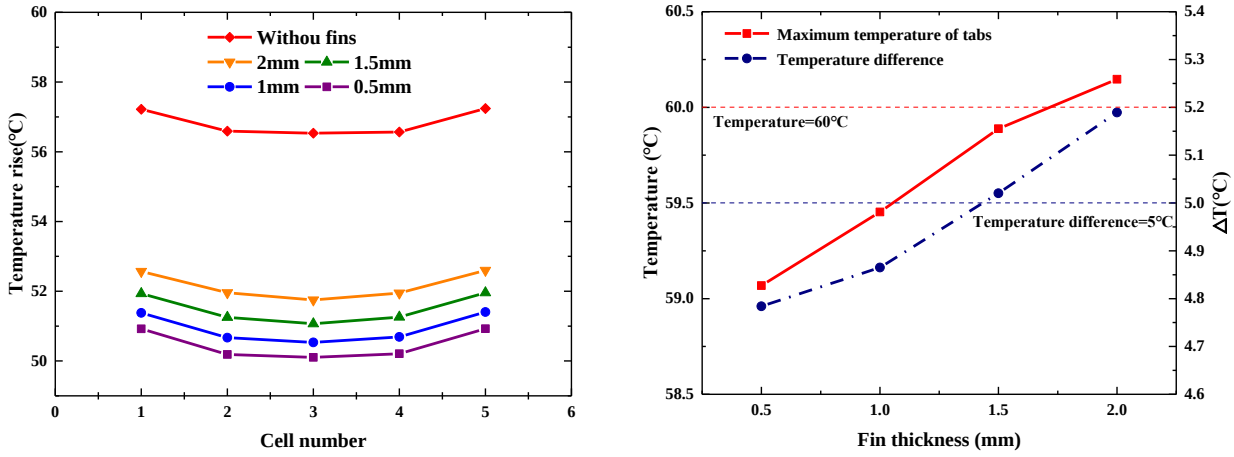

(a) (b)

Fig. 12. (a) Distribution of T_{max} in the module, (b) the maximum temperature of tabs and the temperature difference (ΔT) of the module, with different fin thicknesses at the end of 3C discharge.

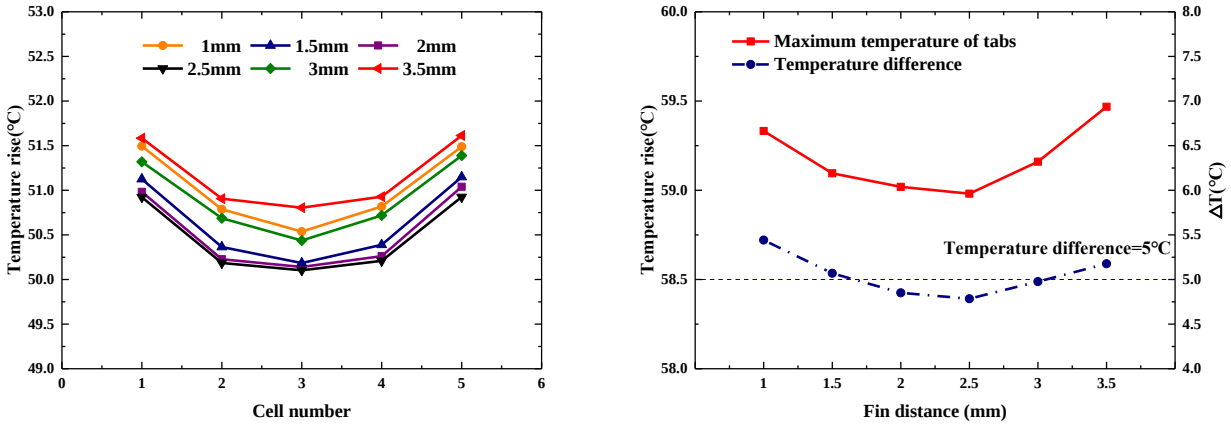

(a) (b)

Fig. 13. (a) Distribution of T_{max} in the module, (b) the maximum temperature of tabs and the temperature difference (ΔT) of the module, with different fin spacing at the end of 3C discharge.

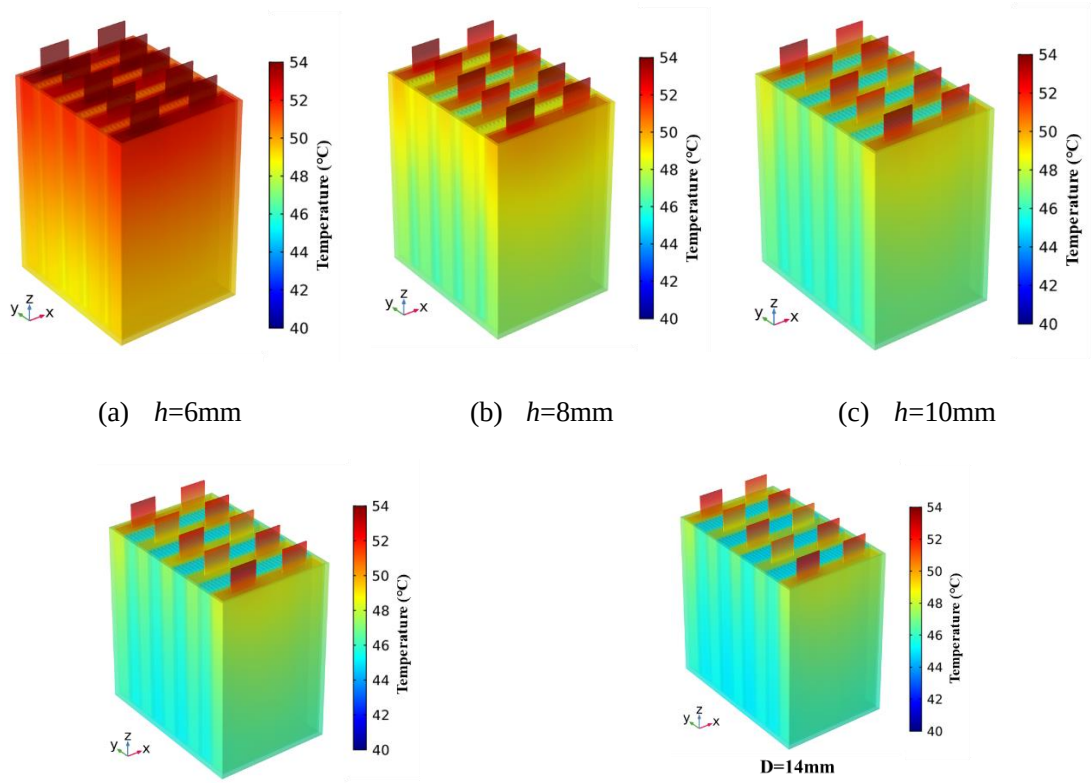

(a) h=6mm (b) h=8mm (c) h=10mm

(d) h=12mm (e) h=14mm

Fig. 14. Temperature contours of module with different PCM thicknesses at the end of 3C discharge.

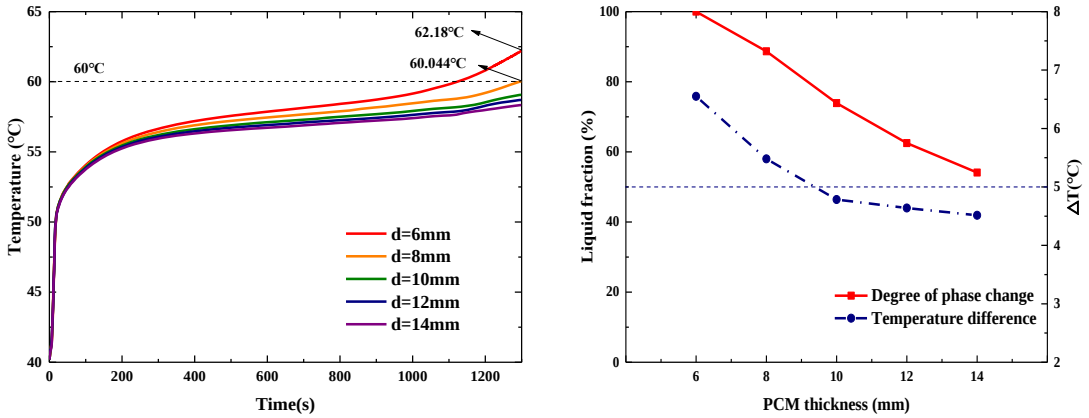

(a) (b)

Fig. 15. (a) Maximum temperature of tabs, (b) Temperature difference (ΔT) of battery module and the PCM liquid fraction, under different PCM thicknesses at the end of 3C discharge.

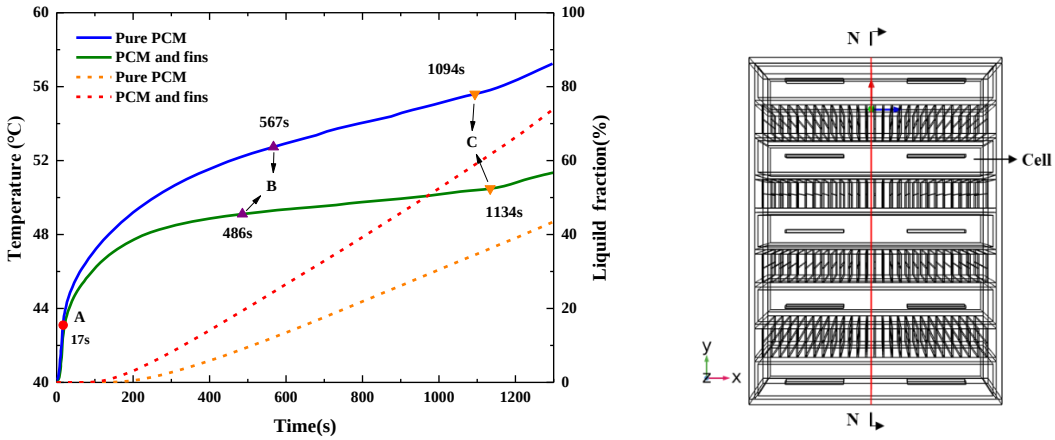

(a) (b)

Fig. 16. (a) Evolution of T_{max} and PCM liquid fraction, (b) schematic of monitored cross section, under the cases of pure PCM and composite PCM-fin structure.

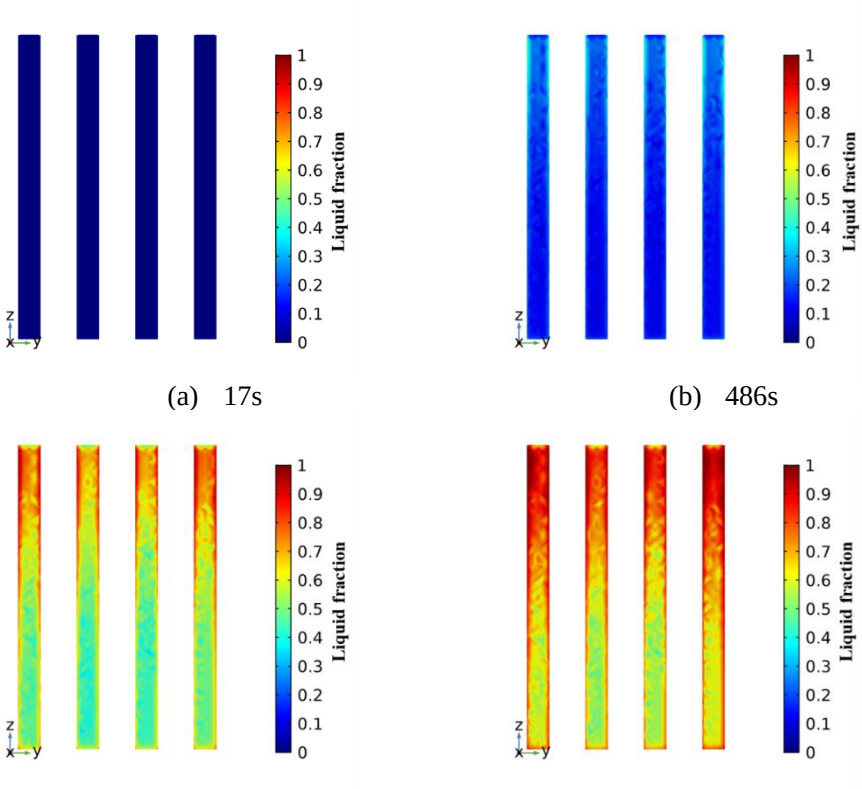

(a) 17s (b) 486s

(c) 1134s (d) End

Fig. 17. The computed liquid fraction in the middle cross section (N-N) of battery module for the case of composite PCM-fin structure at different time points A, B, C and end time.

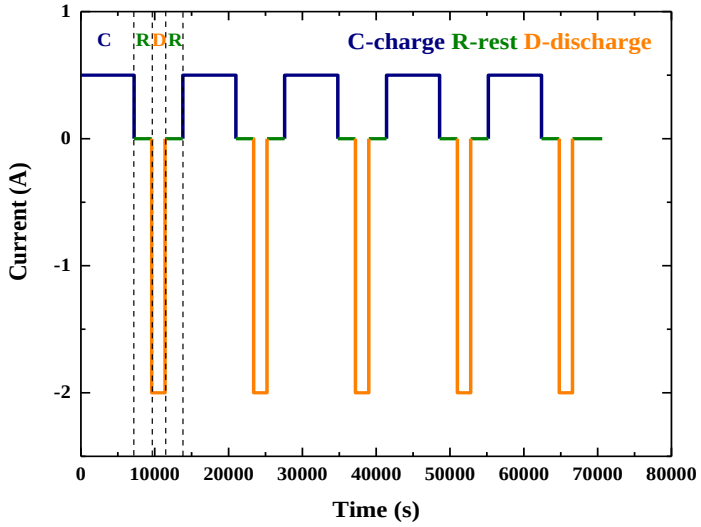

Fig. 18. Testing currents of charge and discharge during the cycles

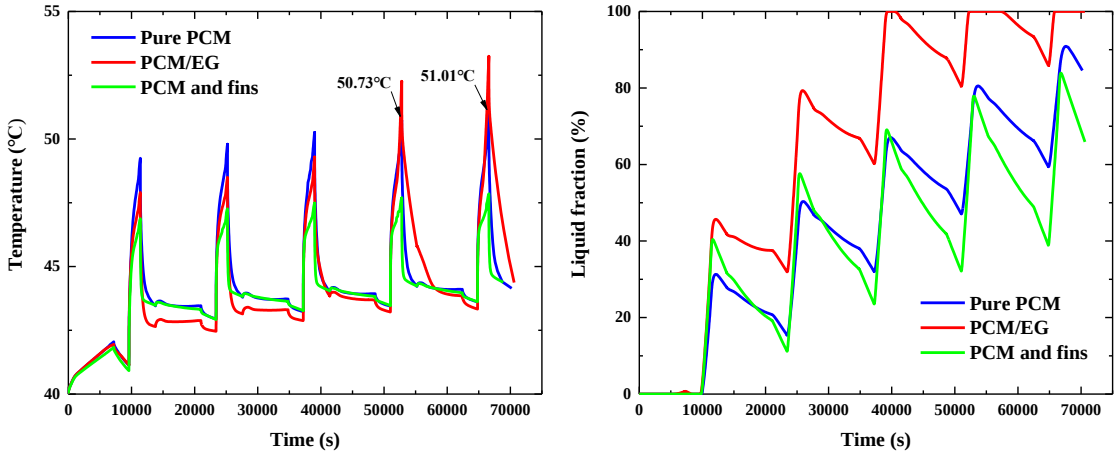

(a) (b)

Fig. 19. (a) Variations of T_{max} with time, (b) Variations of liquid fraction for modules in different thermal management systems during the cycle test.